

3D Macro Physics and Light Odd-Z Element Production in O-C Shell Mergers: Implications for ⁴⁰K production and radiogenic heating inventories of rocky exoplanets

JOSHUA ISSA ^{1,2} FALK HERWIG ^{1,2} STEPHEN J. MOJZSIS ^{3,4,5} AND MARCO PIGNATARI ^{4,5,3,2}

¹*Astronomy Research Centre, Department of Physics & Astronomy, University of Victoria, Victoria, BC, V8W 2Y2, Canada*

²*NuGrid Collaboration, <http://nugridstars.org>*

³*Geoastrometry Research Group, Bayerisches Geoinstitut, Universität Bayreuth, Universitätsstraße 30, 95447 Bayreuth, Germany*

⁴*HUN-REN Research Center for Astronomy and Earth Sciences (CSFK), 1121 Budapest, Konkoly Thege Miklós út 15-17, Hungary*

⁵*CSFK, MTA Centre of Excellence, Budapest, Konkoly Thege Miklós út 15-17., H-1121, Hungary*

(Received XXXXX; Revised YYYYY; Accepted ZZZZZ)

Submitted to ApJ

ABSTRACT

The light odd-Z elements P, Cl, K, and Sc are underproduced in galactic chemical evolution models compared to spectroscopic observations of stars in the Milky Way. The most promising solution to this puzzle is that some massive stars experience O-C shell mergers boosting their yields through dynamic, convective-reactive nucleosynthesis. We report how convective macro physics based on 3D 4π hydrodynamic simulations impacts production in the O shell by post-processing the $M_{\text{ZAMS}} = 15 M_{\odot}$ $Z = 0.02$ model from the NuGrid dataset. We explore a mixing downturn, boosted velocities, reduced ingestion rate, and convective quenching. Across 24 mixing cases, the pre-explosive yields for [P/Fe], [Cl/Fe], [K/Fe], and [Sc/Fe] are modified by $[-0.33, 0.23]$ dex, $[-0.84, 0.64]$ dex, $[-0.78, 1.48]$ dex, and $[-0.36, 1.29]$ dex, respectively. Cases with a convective downturn with the fastest ingestion rate have the largest enhancement, and production is non-monotonic with boosted velocities. Which reactions are most important for the convective-reactive element production pathways depends on the mixing case. We parameterize production of ⁴⁰K ($t_{1/2} = 1.248$ Gyr), an important radiogenic heat source for younger (2–3 Gyr) rocky planets and find a yield variation exceeding three orders of magnitude. This range of initial abundances for ⁴⁰K implies the early geodynamic behaviour of silicate mantles in rocky planets can differ greatly from that of Earth. These results underscore the importance of investigating the 3D macro physics of shell merger convection through hydrodynamic simulations to develop a predictive understanding of the origin and variability of the light odd-Z elements and the ⁴⁰K/K ratio in planet host stars.

Keywords: Massive stars (732) — Oxygen burning (1193) — Stellar convective shells (300) — Nuclear astrophysics (1129) — Exoplanets (498) — Planetary atmospheres (1244)

1. INTRODUCTION

The radiogenic isotope ⁴⁰K with a half-life of 1.248 Gyr is the dominant heat-producing nuclide for rocky exoplanets in the first few billion years of their geologic histories (e.g. C. O’Neill et al. 2020), with Earth as the baseline example (J. Korenaga 2008). Of the long-lived radionuclides present in silicate mantles of rocky planets, ⁴⁰K-driven radiogenic heating contributes to mantle convection that feeds into volcanism, the pri-

mary mechanism for transferring volatiles from planetary interiors to atmospheres. Variations in initial ⁴⁰K inventories directly affect the duration and intensity of volcanic degassing (L. Noack & D. Breuer 2014), particularly during the critical first 2–3 billion years when secondary atmosphere formation occurred when ⁴⁰K was still a dominant heat-producer (T. P. Fischer & A. Aiuppa 2020).

Therefore, any model of the geodynamic evolution of rocky exoplanets requires knowledge of the initial ⁴⁰K inventories. However, K belongs to a group of elements with a particularly uncertain production history. A long-standing problem has been that the light odd-Z

elements P, Cl, K, and Sc are produced in insufficient quantities in galactic chemical evolution (GCE) models. Indeed, GCE models predict that the majority contribution for these elements comes from core-collapse supernovae (CCSNe), but they cannot match observed stellar abundances (e.g. T. Mishenina et al. 2017; N. Prantzos et al. 2018; C. Kobayashi et al. 2020). A recent realization has been that the light odd-Z elements are significantly produced during O-C shell merger in massive stars prior to a CCSN at all metallicities (T. Rauscher et al. 2002; C. Ritter et al. 2018a; L. Roberti et al. 2025), and GCE models including this effect parametrically can match stellar abundance observations.

Current K and by extension ^{40}K predictions from O-C shell mergers remain uncertain. A key source of uncertainty is the impact of macro physics of convection during the dynamic nucleosynthesis, possibly with feedback, as demonstrated recently for the p -process-production in O-C shell mergers (J. Issa et al. 2025). A ^{40}K production variability similar to that seen for p -process abundance predictions taking into account different scenarios of macro physics of convection based on stellar hydrodynamics simulations, could lead to divergent planetary atmospheric evolution pathways. Differences in composition and thickness of planet atmospheres depend on both the thermal state driving outgassing efficiency and the pressure-temperature conditions controlling volatile speciation (G. Ortenzi et al. 2020), creating potentially observable signatures in $\text{CO}_2/\text{H}_2\text{O}$ ratios and atmospheric oxidation states that future missions like the Habitable Worlds Observatory could detect (P. Liggins et al. 2022a). A predictive, quantitative understanding of ^{40}K production would remove a key roadblock in our ability to model the thermal evolution of silicate-metal exoplanets (E. A. Frank et al. 2014).

Not really surprising, three-dimensional (3D) hydrodynamic simulations of the O shell where the nucleosynthesis occurs show very different mixing conditions compared to one-dimensional (1D) predictions using mixing length theory (MLT) (C. A. Meakin & D. Arnett 2006, 2007; S. Jones et al. 2017; R. Andrassy et al. 2020; N. Yadav et al. 2020; F. Rizzuti et al. 2024). These simulations have shown that the radial mixing efficiency profile has a downturn as the convective boundary is approached, which is not captured in 1D models which predict the mixing should be nearly constant across the convective shell (C. A. Meakin & D. Arnett 2006, 2007; S. Jones et al. 2017). They also predict that the convective velocities could be larger by up to a factor of 30 or more than what is predicted by 1D models (S. Jones et al. 2017; R. Andrassy et al. 2020; F. Rizzuti et al. 2024). Finally, convective quenching due to en-

ergy feedback from the ingestion of fresh fuel has been demonstrated in 3D simulations of H-ingestion in post-AGB (asymptotic giant branch; AGB) stars (F. Herwig et al. 2014), and the ingestion of C-shell material into the O shell may play a similar restricting role in O-C shell mergers (R. Andrassy et al. 2020).

These mixing conditions directly affect the nucleosynthesis as the O shell is a convective-reactive environment where the timescales for mixing and burning are comparable (C. Ritter et al. 2018a; N. Yadav et al. 2020; F. Rizzuti et al. 2024). F. Rizzuti et al. (2024) have shown in their 3D simulation of an O-C shell merger that all isotopes have significantly different results compared to 1D simulations.

Here we consider how the isotopes ^{31}P , $^{35,37}\text{Cl}$, $^{39,40,41}\text{K}$, and ^{45}Sc are produced in the O shell and how it is impacted by the mixing conditions. This extends the work done by J. Issa et al. (2025) that analyzed how the p nuclei are affected by the mixing conditions during the shell merger. We analyze the production of these nuclides, with special attention to K and its isotopes. While stellar spectral data of the host star can be used to infer plausible major element compositions of rocky exoplanets (e.g. R. J. Spaargaren et al. 2023), only GCE models can provide likely relative abundances of the radioactive nuclides (^{40}K , ^{232}Th , $^{235-238}\text{U}$), tied to the age of that system, that can be used to infer heat production in the interiors of rocky exoplanets (E. A. Frank et al. 2014). While indeed for Th it is possible to directly observe ^{232}Th in stars in the Milky Way disk, current spectroscopic observation uncertainties still hinder precise derivation of its abundances (e.g., R. B. Botelho et al. 2019; T. Mishenina et al. 2022, and references therein).

This paper is structured as follows. In §2, we describe our methodology, including the initial conditions from the NuGrid stellar model, the post-processed models with different mixing scenarios, and our approach for estimating final yields and reaction contributions. §3 presents our main results, focusing on the nucleosynthesis of light odd-Z isotopes and how different mixing conditions impact their production. In §4, we discuss the production of ^{40}K and its implications for heterogeneous pollution of the interstellar medium and radiogenic heating in rocky exoplanets. Finally, §5 provides our discussion and conclusions, highlighting the importance of mixing conditions for understanding the origin of light odd-Z elements, their impact on galactic chemical evolution models and radiogenic heating in rocky exoplanets.

2. METHODOLOGY

2.1. The O-C shell merger model

The radial stratification for the O shell multizone nucleosynthesis simulations in this paper are taken from the non-rotating, 1D 15 M_{\odot} , $Z = 0.02$ massive star model from C. Ritter et al. (2018b) calculated with the MESA stellar evolution code (B. Paxton et al. 2010) and post-processed with the multizone NuGrid code mppnp (M. Pignatari et al. 2016). This model does not have exponential-diffusive convective boundary mixing (B. Freytag et al. 1996; F. Herwig 2000) after the cessation of core He burning (which was explored in A. Davis et al. 2018). The evolution of the convection zones is shown in a Kippenhahn diagram (Figure 1) in J. Issa et al. (2025). The light odd-Z elements are mildly produced in the first convective O shell, which extends from 1.55 M_{\odot} to 1.95 M_{\odot} during a time interval $\log_{10}(t - t_{\text{end}})/\text{yr} = -1.76$ to -2.16 , but the O-C shell merger at $\log_{10}(t - t_{\text{end}})/\text{yr} = -3.85$ is the dominant source of the elements (C. Ritter et al. 2018a).

Table 1 summarizes the NuGrid model properties with O-C shell mergers from C. Ritter et al. (2018b). The 12, 15, and 20 M_{\odot} models show clear differences in the size of the merged shells Δm , duration of the merger Δt , and overproduction factors OP for $^{39-41}\text{K}$. However, both 15 M_{\odot} models with metallicities $Z = 0.01$ and $Z = 0.02$ are quite similar in all these properties, including in OP, although the $Z = 0.02$ model produces three times more ^{39}K by the end of the merger because of a higher initial mass fraction. This would suggest that initial mass of the star is more determinate of the merger and its nucleosynthesis than its metallicity. In fact, L. Roberti et al. (2025) shows that models with O-C shell mergers do not have a general trend in $[\text{K}/\text{Mg}]$ across metallicities of $Z = 10^{-9}$ – 10^{-2} .

2.2. Post-Processed Models

We build on the post-processing models from J. Issa et al. (2025) that use results from 3D hydrodynamic simulations to motivate mixing scenarios expressed in terms of mixing efficiency profiles that are different from the MLT 1D predictions. These scenarios are described in detail in J. Issa et al. (2025) and are summarized here. The MLT mixing case has a mixing efficiency profile essentially constant across the O shell as taken from C. Ritter et al. (2018b). The 3D simulations, however, predict a mixing efficiency downturn as the convective boundary is approached and also suggest a boost to the mixing efficiencies of 1, 3, 10, and 50 (C. A. Meakin & D. Arnett 2007; S. Jones et al. 2017; R. Androssy et al. 2020; F. Rizzuti et al. 2024), to some degree depending on the uncertain hydrodynamic response to the

ingestion and burning of additional nuclear fuel. The quenched mixing cases consider a dip in the mixing efficiency profile which also may arise due to energy feedback in the middle of the shell and partial merging of the shells at the top (R. Androssy et al. 2020). The MLT and 3D-inspired mixing cases are calculated for a range of ingestion rates from $4 \times 10^{-5} M_{\odot}\text{s}^{-1}$, $4 \times 10^{-4} M_{\odot}\text{s}^{-1}$, $4 \times 10^{-3} M_{\odot}\text{s}^{-1}$, again reflecting our limited knowledge of as well as intrinsically varying conditions in real 3D stars. A case without ingestion is also included for reference. The ingestion rates are consistent with those adopted in 3D simulations of R. Androssy et al. (2020). The extent of the C shell is 0.8 M_{\odot} , so for a post-processing simulation time of 110 s (corresponding roughly to a convective turnover time), the maximum ingestion rate would be $7 \times 10^{-3} M_{\odot}\text{s}^{-1}$ like C. Ritter et al. (2018a). Our fastest ingestion rate of $4 \times 10^{-3} M_{\odot}\text{s}^{-1}$ reflects a full merger. The quenched mixing cases are calculated with an ingestion rate of $4 \times 10^{-3} M_{\odot}\text{s}^{-1}$ only. Care has been taken that our post-processing models are converged with respect to spatial and temporal resolution (J. Issa et al. 2025).

2.3. Estimating Pre-Explosive Yields

The post-processed models in this work are calculated only for the O shell and do not include the full stellar structure, however to estimate what the final yields would be if the mixing prescriptions were implemented in stellar evolution, we take the following approach. The final ejected mass of a species i is given by:

$$\text{EM}_i = \text{EM}_i^{\text{wind}} + \text{EM}_i^{\text{SN}}$$

where $\text{EM}_i^{\text{wind}}$ are the yields from winds throughout stellar evolution and EM_i^{SN} are the ejected yields due to a supernova without explosive burning as described by C. Ritter et al. (2018b). Winds are taken from the surface abundances and are not affected by the mixing conditions in the O shell, but the pre-explosive supernova yields are. To estimate this, we assume that the ratio of the decayed mass fractions calculated in our models at $t = 110$ s to those in the C. Ritter et al. (2018b) O shell at $\log_{10}(t - t_{\text{end}})/\text{yr} = -3.856$ remains the same for the whole merger across the whole O-C region. This approximation of what the yields of an entire stellar model would be if it incorporated into stellar evolution neglects the changing temperature and density as the merger proceeds and feedback effects from the burning of ingested C-shell material. Following C. Ritter et al. (2018b), a delayed explosion mass cut at $m = 1.61 M_{\odot}$ is used:

$$\text{EM}_i^{\text{SN}} = \int_{1.61 M_{\odot}}^{2.95 M_{\odot}} X_i \cdot \text{ratio}_i dm + \int_{2.95 M_{\odot}}^{m_{\tau}} X_i dm$$

M_{ZAMS}	Z_{ini}	Δm	Δt	$\langle X(^{39}\text{K}) \rangle_{\text{fin}}$	OP(^{39}K)	$\langle X(^{40}\text{K}) \rangle_{\text{fin}}$	OP(^{40}K)	$\langle X(^{41}\text{K}) \rangle_{\text{fin}}$	OP(^{41}K)
12 M_{\odot}	0.01	0.6 M_{\odot}	0.029 h	2.48×10^{-4}	1.531	6.72×10^{-6}	1.362	1.49×10^{-6}	0.487
15 M_{\odot}	0.01	1.52 M_{\odot}	0.74 h	3.01×10^{-4}	1.98	3.24×10^{-5}	1.934	2.71×10^{-5}	1.63
20 M_{\odot}	0.01	3.6 M_{\odot}	5.43 h	2.28×10^{-4}	1.841	3.56×10^{-6}	0.895	7.01×10^{-7}	0.004
15 M_{\odot}	0.02	1.43 M_{\odot}	1.252 h	9.43×10^{-4}	2.028	5.85×10^{-5}	1.965	2.38×10^{-5}	1.305

Table 1. Properties of the merger and production of K for the NuGrid models with O-C shell mergers. The averaged mass fractions are within the maximum extent of the merger region and $\text{OP} = \log_{10}(\langle X_{\text{fin}} \rangle / \langle X_{\text{ini}} \rangle)$ where $\langle X_{\text{ini}} \rangle$ and $\langle X_{\text{fin}} \rangle$ are taken at the start and end of the merger. Note that the models have different initial mass fractions of $^{39-41}\text{K}$.

where X_i is the mass fraction of an element i , m_{τ} is the extent of the star at collapse, and 1.61–2.95 M_{\odot} is the O-C merger region above the mass-cut. The mass fraction is calculated as the yield of a given species normalized to the total yield:

$$X_i = \text{EM}_i \div \sum_i^N \text{EM}_i \quad (1)$$

where N is the total number of species.

The final results are calculated in square bracket notation against C. Ritter et al. (2018b) (indicated by the subscript ref = R) and the solar measurements from M. Asplund et al. (2009) (ref = \odot):

$$[\text{X}/\text{Y}]_{\text{norm}} = \log_{10}(\text{X}/\text{Y})_{\text{norm}} - \log_{10}(\text{X}/\text{Y})_{\text{ref}}$$

where X and Y are mass fractions calculated with Eq. (1), and the subscript norm is what is being compared to the reference value.

2.4. Estimating Reaction Contribution

The reaction flux f_{ij} is defined as the net flux of the reaction between species i and j :

$$f_{ij} = \frac{X_i X_j}{A_i A_j} \rho N_A \left(\langle \sigma v \rangle_{ij} - \langle \sigma v \rangle_{ji} \right)$$

where X is the mass fraction, A is the atomic mass, ρ is the density, N_A is Avogadro's number, and $\langle \sigma v \rangle_{ij}$ is the reaction rate between species i and j .

To estimate the total contribution of a reaction to the production and destruction of a species, we calculate the average reaction flux F_{ij} over mass and time:

$$F_{ij} = \frac{1}{\delta t (m_{\text{top}} - m_{\text{bot}})} \int_{t_c}^{t_c + \delta t} \int_{m_{\text{bot}}}^{m_{\text{top}}} |f_{ij}(m, t)| dm dt$$

Using this, we can define what percentage a particular reaction i contributes to the total flux for a species:

$$\langle \text{contribution} \rangle_i = \frac{F_j}{\sum_j F_{ij}} \quad (2)$$

calculated at $t_c = 110$ sec and $\delta t = 1$ sec. This provides quasi-equilibrium reaction fluxes at the end of the simulation.

3. RESULTS

3.1. Nucleosynthesis of the light odd-Z isotopes

The reference case is the nucleosynthesis of the light odd-Z isotopes in the O shell with the MLT-based mixing efficiency profile with an ingestion rate of $4 \times 10^{-3} M_{\odot} \text{s}^{-1}$. ^{16}O produces p , n , and α by the main O-burning reaction $^{16}\text{O} + ^{16}\text{O}$, but the ingestion of ^{12}C adds to the p , n , and α release by $^{12}\text{C} + ^{12}\text{C}$ and $^{12}\text{C} + ^{16}\text{O}$ reactions at O-burning temperatures. The sudden increase of p , n , and α increases the capture reactions (p, γ) , (n, γ) , (α, γ) , (α, p) , and (p, α) significantly which is one of the reasons why the light odd-Z elements are produced much more during the merger than the first (cf. §2.1) convective O shell.

The main reaction channels are shown in Fig. 1. Many additional reactions that are not shown as the convective-reactive nature of the O shell means different locations in the shell have varying contributions. Fig. 2 shows the isotopic mass fractions across the O shell, and as it shows the light odd-Z isotopes have a peak 1.6–1.7 M_{\odot} .

Important isotopes like ^{30}Si , $^{32,34}\text{S}$, and ^{38}Ar are created in the first convective O shell, and ^{37}Cl , ^{40}Ar , and ^{44}Ca are created in the C shell and ingested during the merger. These pathways were determined by analyzing the production of each of the species during the evolution of the C. Ritter et al. (2018b) model and the fluxes in our post-processed models. The only stable P isotope ^{31}P is produced by $^{16}\text{O}(^{16}\text{O}, p)^{31}\text{P}$. The stable Cl isotope ^{35}Cl is produced by $^{30}\text{Si}(\alpha, \gamma)^{34}\text{S}(p, \gamma)^{35}\text{Cl}$, $^{32}\text{S}(\alpha, p)^{35}\text{Cl}$, and $^{35}\text{S}(p, n)^{35}\text{Cl}$. ^{37}Cl is both ingested from the C shell and produced by $^{34}\text{S}(p, \alpha)^{37}\text{Cl}$ and $^{35}\text{Cl}(n, \gamma)^{36}\text{Cl}(n, \gamma)^{37}\text{Cl}$. The principal stable isotope of K, ^{39}K is produced by $^{38}\text{Ar}(p, \gamma)^{39}\text{K}$, the long-lived radioisotope ^{40}K is produced by $^{39}\text{K}(n, \gamma)^{40}\text{K}$, and the other stable K isotope ^{41}K is produced by $^{40}\text{K}(n, \gamma)^{41}\text{K}$ and $^{40}\text{Ar}(p, \gamma)^{41}\text{K}$. Finally, the only stable Sc isotope ^{45}Sc is produced by $^{38}\text{Ar}(\alpha, \gamma)^{42}\text{Ca}(n, \gamma)^{43}\text{Ca}(n, \gamma)^{44}\text{Ca}(p, \gamma)^{45}\text{Sc}$. However, our analysis shows that different reactions dominant the light odd-Z isotopic production depending on the mixing conditions as shown in Tables 2 and 3. Ad-

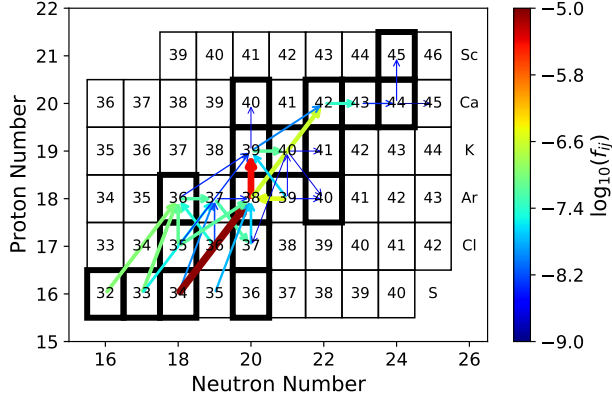


Figure 1. Chart of reactions between isotopes at $m = 1.65 M_{\odot}$ [$T = 2.231$ GK] for the MLT mixing case with an ingestion rate of $4 \times 10^{-3} M_{\odot} s^{-1}$ at $t = 110$ s. Both arrow colour and size indicate $\log_{10}(f_{ij})$, and arrows point in the direction of the reaction.

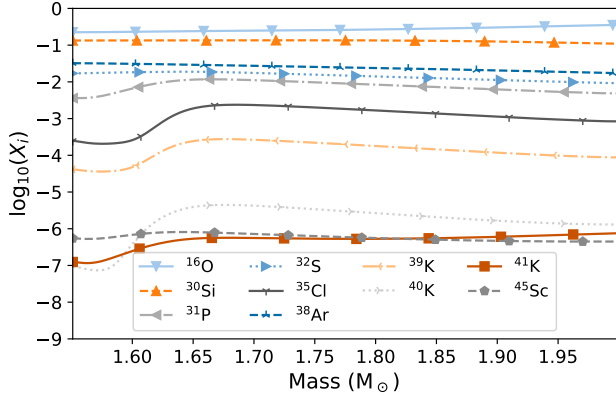


Figure 2. Isotopic mass fractions at $t = 110$ s without decays for the MLT mixing case with an ingestion rate of $4 \times 10^{-3} M_{\odot} s^{-1}$.

ditionally, the transient before the quasi-equilibrium at the end of the simulation will have different dominant reactions, but we assume that this is not important for the final yields.

3.2. Impact of macro physics mixing on light odd-Z nucleosynthesis production

Fig. 3 shows the spread across all 24 mixing cases in overproduction in the O shell only at the end of the merger, $OP = \log_{10}(X_i/X_{i,ini})$, where X_i is the final decayed, mass-averaged mass fraction of an isotope and $X_{i,ini}$ is the initial mass fraction at the start of the merger. Over the range of mixing scenarios and entrainment rates, ^{31}P has a spread $OP_{\max} - OP_{\min}$ of 0.58 dex, ^{35}Cl has 1.76 dex, ^{37}Cl has 0.81 dex, ^{39}K has 2.42 dex, ^{40}K has 3.37 dex, ^{41}K has 2.31 dex,

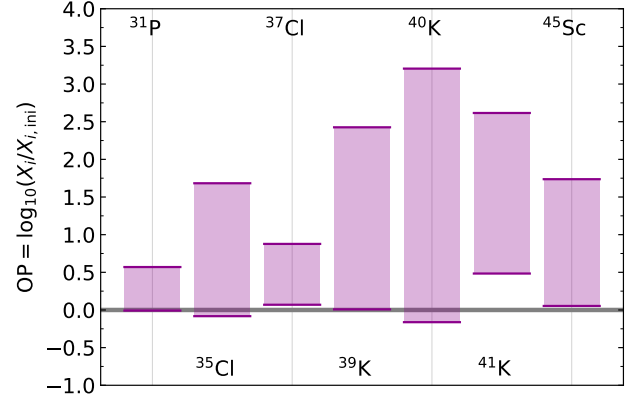


Figure 3. Overproduction of the light odd-Z isotopes for all 24 mixing cases in the O shell at 110 s. The average spread $OP_{\max} - OP_{\min} = 1.82$ dex, and the line at $OP = 0$ is the initial amount.

and ^{45}Sc has 1.68 dex with an average spread across all light odd-Z isotopes of 1.82 dex. The K isotopes are the most affected by the mixing conditions, and ^{40}K has the largest spread of all isotopes. This underscores the importance of understanding the 3D macro physics from hydrodynamic simulations to reliably predict the final production during a merger.

Figures 4–7 show the modification to the pre-explosive yields of C. Ritter et al. (2018b) as described in §2.3. The ratios $[\text{P}/\text{Fe}]$, $[\text{Cl}/\text{Fe}]$, $[\text{K}/\text{Fe}]$, and $[\text{Sc}/\text{Fe}]$ are changed by $[-0.33, 0.23]$ dex, $[-0.84, 0.64]$ dex, $[-0.78, 1.48]$ dex, and $[-0.36, 1.29]$ dex respectively. The elemental abundances are most enhanced for the fastest ingestion rate of $4 \times 10^{-3} M_{\odot} s^{-1}$ and for the mixing cases with a downturn in the mixing efficiency. This enhancement is non-monotonic with increasing convective velocities for all elements except K which is indeed most enhanced for the $50 \times D_{3D-\text{insp.}}$ mixing case.

Isotopes of the same element are not affected the same way by the mixing conditions (Fig. 3), and therefore elemental and isotopic enhancements are not necessarily aligned. Elemental K has the largest enhancement for the $50 \times D_{3D-\text{insp.}}$ mixing case (Fig. 6), but the isotope ^{40}K is most enhanced for the 1 and $3 \times D_{3D-\text{insp.}}$ mixing cases (Fig. 8). Elemental K is primarily ^{39}K . The enhancement of ^{40}K in the lower mixing cases implies that the mixing conditions affect how these isotopes are produced relative to each other.

Mixing conditions affect nucleosynthesis in a non-monotonic way because the O shell is a convective-reactive environment. As explored in J. Issa et al. (2025), when the mixing speeds change, so does the location of peak burning. For example, consider the reactions contributing to the ^{40}K mass fraction for the MLT

Isotope	$^{16}\text{O}(^{16}\text{O},p)$	(α,γ)	(α,n)	(α,p)	(p,γ)	(p,n)	(n,γ)	(γ,n)	(γ,p)	(n,p)	(n,α)	(p,α)
^{31}P	+0.97			-0.01	+0.01							
^{35}Cl		+0.01		+0.18	-0.57	+0.22		-0.01	+0.01			
^{37}Cl				+0.23	+0.07		+0.02		-0.45	+0.22		
^{39}K		+0.02		+0.04	-0.71	+0.14		-0.05	+0.01			-0.02
^{40}K			-0.09		+0.03	-0.05	+0.64	-0.09	-0.04	-0.05		
^{41}K		+0.1		-0.28	+0.24		+0.18		-0.03	-0.17		
^{45}Sc					+0.49	+0.01		-0.07	-0.42			

Table 2. Reaction fluxes contributing to the light odd-Z isotopes using Eq. (2) for the MLT mixing case with an ingestion rate of $4 \times 10^{-3} \text{ M}_{\odot} \text{ s}^{-1}$. Contributions starting with + are productive (should be read as $i \rightarrow j$ eg. $^{34}\text{S}(p,\gamma)^{37}\text{Cl}$ with +0.23), those starting with - are destructive (should be read as $i \leftarrow j$ eg. $^{34}\text{S}(p,\gamma)^{35}\text{Cl}$ with -0.57), and those left blank contribute less than 1%.

Isotope	$^{16}\text{O}(^{16}\text{O},p)$	(α,γ)	(α,n)	(α,p)	(p,γ)	(p,n)	(n,γ)	(γ,n)	(γ,p)	(n,p)	(γ,α)	(n,α)	(p,α)
^{31}P	+0.91			-0.04	+0.02				-0.01			-0.01	
^{35}Cl				+0.05	-0.9	+0.01			-0.03			-0.01	
^{37}Cl				-0.06	+0.03				-0.52	+0.38			
^{39}K				+0.01	-0.96				-0.01			-0.01	
^{40}K			-0.02	-0.03	+0.02	-0.01	+0.33	-0.02	-0.2	-0.37			
^{41}K		+0.11		-0.33	+0.2		+0.15		-0.05	-0.15	+0.01		
^{45}Sc				+0.08	+0.29		+0.01	-0.02	-0.49	+0.1			

Table 3. Reaction fluxes contributing to the light odd-Z isotopes using Eq. (2) for the $50 \times D_{3\text{D-insp.}}$ mixing case with an ingestion rate of $4 \times 10^{-3} \text{ M}_{\odot} \text{ s}^{-1}$. Contributions starting with + are productive (should be read as $i \rightarrow j$ eg. $^{39}\text{K}(n,\gamma)^{40}\text{K}$ with +0.33), those starting with - are destructive (should be read as $i \leftarrow j$ eg. $^{40}\text{Ca}(n,p)^{40}\text{K}$ with -0.37), and those left blank contribute less than 1%.

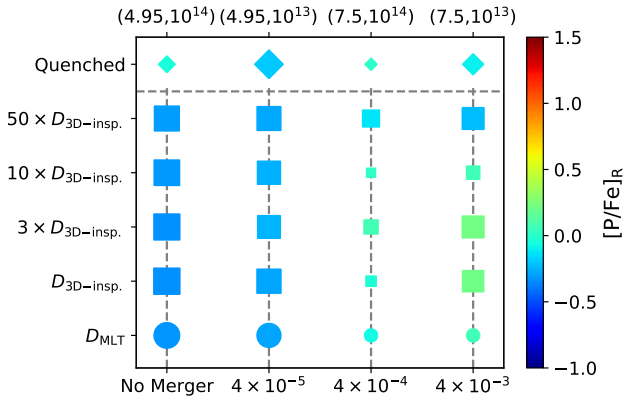


Figure 4. The change in dex for $[\text{P}/\text{Fe}]$ to the $M_{\text{ZAMS}} = 15 \text{ M}_{\odot}$, $Z = 0.02$ model from C. Ritter et al. (2018b) as described in §2.3. The lower x-axis is the ingestion rate in $\text{M}_{\odot} \text{ s}^{-1}$ for the MLT (circles) and 3D-inspired mixing (squares) cases. The upper x-axis is the centre of the mixing efficiency dip in Mm and the extent of the dip in $\text{cm}^2 \text{ s}^{-1}$ for the quenched (diamonds) mixing cases. Size indicates distance from $[\text{P}/\text{Fe}]_{\text{R}} = 0$, and colour indicates the magnitude. The delayed pre-explosive $[\text{P}/\text{Fe}]_{\odot}$ for the C. Ritter et al. (2018b) model is 2.13 dex.

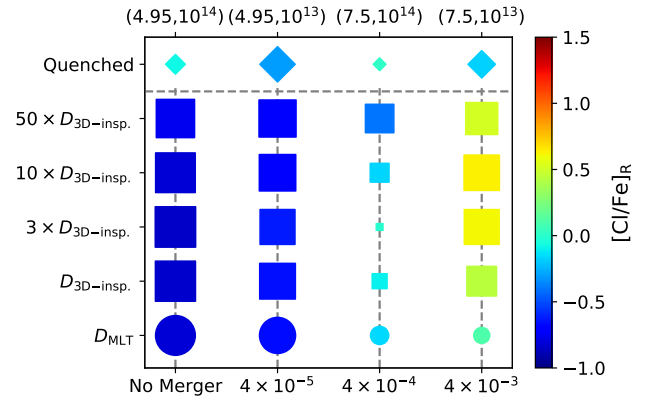


Figure 5. The same as Fig. 4 but for $[\text{Cl}/\text{Fe}]_{\text{R}}$. The delayed pre-explosive $[\text{Cl}/\text{Fe}]_{\odot}$ for the C. Ritter et al. (2018b) model is 2.14 dex.

mixing case in Fig. 9 and the $50 \times D_{3\text{D-insp.}}$ mixing case in Fig. 10.

Comparing Figures 9 and 10 we see that for the faster mixing case (1) the reaction fluxes $\log_{10}(f_{ij})$ are stronger (2) the mass fractions X_i are higher and have a different shape (3) the location of the strongest reactions are deeper in the shell (4) the dominant reactions are dif-

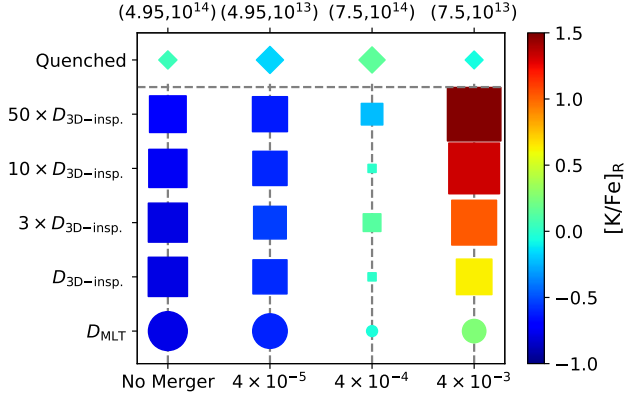


Figure 6. The same as Fig. 4 but for $[K/Fe]_R$. The delayed pre-explosive $[K/Fe]_\odot$ for the C. Ritter et al. (2018b) model is 1.59 dex.

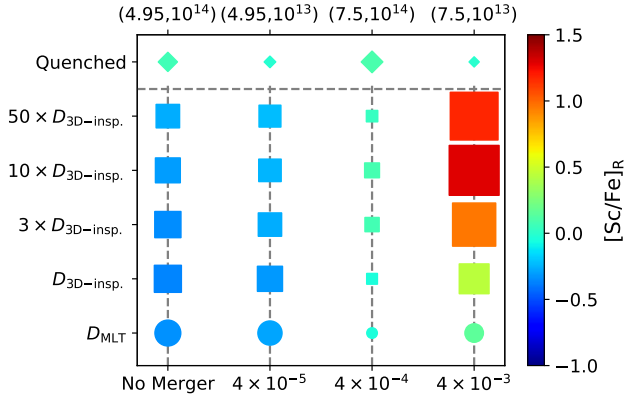


Figure 7. The same as Fig. 4 but for $[Sc/Fe]_R$. The delayed pre-explosive $[Sc/Fe]_\odot$ for the C. Ritter et al. (2018b) model is 1.79 dex.

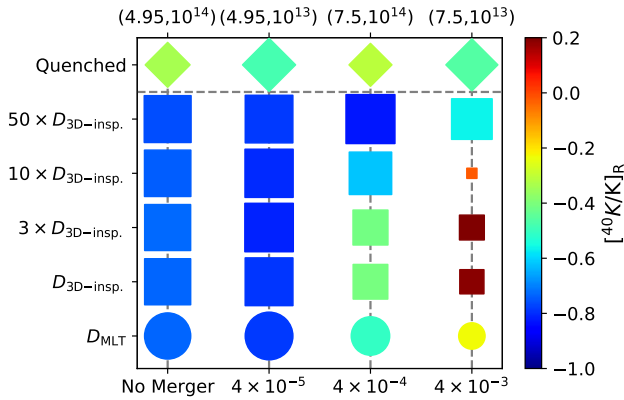


Figure 8. The same as Fig. 4 but for $[^{40}\text{K}/K]_R$. The delayed pre-explosive $[^{40}\text{K}/K]_\odot$ for the C. Ritter et al. (2018b) model is 1.65 dex. Note that the colourbar is different from Figures 4–7.

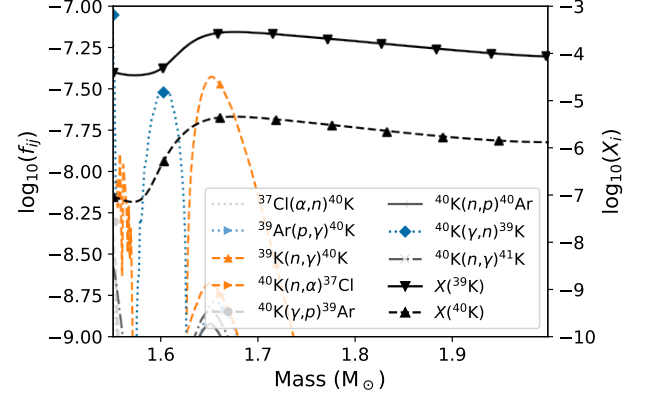


Figure 9. Reaction fluxes f_{ij} for ^{40}K and mass fractions X_i for $^{39,40}\text{K}$ for the MLT mixing case with an ingestion rate of $4 \times 10^{-3} \text{ M}_\odot \text{ s}^{-1}$ at $t = 110 \text{ s}$. The direction of reactions $i \rightarrow j$ are written as left to right in the legend. Note that the reaction direction notation as always left to right is different than Table 2.

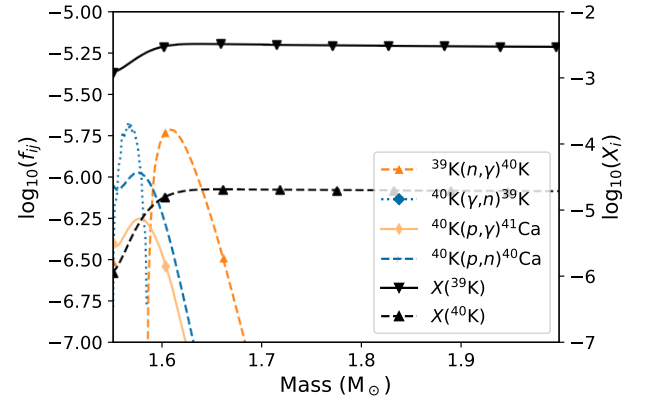


Figure 10. The same as Fig. 9 but for the $50 \times D_{3D-insp.}$ mixing case with an ingestion rate of $4 \times 10^{-3} \text{ M}_\odot \text{ s}^{-1}$. Note that the reaction direction notation as always left to right is different than Table 3.

ferent. In both cases, ^{40}K is both produced and destroyed by $^{39}\text{K}(n,\gamma)^{40}\text{K}$, but in the faster mixing case these reactions occur at hotter temperatures deeper in the shell and the destructive terms $^{40}\text{K}(p,n)^{40}\text{Ca}$ and $^{40}\text{K}(p,\gamma)^{41}\text{Ca}$ are much stronger. Note that ^{40}K is being net destroyed in the faster mixing case, but still has a higher mass fraction because ^{39}K is being produced even more. This is evident when comparing to Fig. 8 where the $50 \times D_{3D-insp.}$ mixing case has a lower $[^{40}\text{K}/K]$ ratio than the MLT case. Since the shell is convective-reactive, the nucleosynthesis is sensitive to the ratio of the timescales for mixing and burning which changes the location where reactions peaks occur. This behaviour is relevant for all nucleosynthesis in the O shell and is the

cause of the spread in Fig. 3 and elemental abundance enhancements in Figures 4–7.

4. HETEROGENEOUS ^{40}K INTERSTELLAR MEDIUM ENRICHMENT AND IMPACT FOR ROCKY PLANET HEATING

As discussed in the previous sections, all K isotopes are efficiently produced in O-C shell mergers. It is known that this could reconcile the $[\text{K}/\text{Fe}]$ observations in the Milky Way disk with GCE simulations (C. Ritter et al. 2018a). ^{40}K receives the biggest boost compared to the solar scaled initial abundances. Let's consider as example the 15 M_{\odot} $Z = 0.02$ model by C. Ritter et al. (2018a), affected by O-C shell merger, and the analogous non-rotating model in the stellar set by M. Limongi & A. Chieffi (2018). The ^{39}K , ^{40}K and ^{41}K yields by the model with O-C shell merger are $1.959 \times 10^{-3}\text{ M}_{\odot}$, $1.165 \times 10^{-4}\text{ M}_{\odot}$ and $6.694 \times 10^{-5}\text{ M}_{\odot}$, respectively. The model without O-C shell merger ejects $1.061 \times 10^{-4}\text{ M}_{\odot}$, $6.071 \times 10^{-7}\text{ M}_{\odot}$ and $1.046 \times 10^{-5}\text{ M}_{\odot}$, respectively. While ^{39}K and ^{41}K boosts are in the order of a factor of 10 or less (C. Ritter et al. 2018a), the ^{40}K increase in our 1D model with O-C shell merger is almost 200 times larger compared to a standard CCSN production seen in the model by M. Limongi & A. Chieffi (2018). Additionally, we consider yields from our most enhanced ^{40}K production cases, the $10 \times D_{3\text{D-insp.}}$ case with an ingestion rate of $4 \times 10^{-3}\text{ M}_{\odot}$, which should be considered as an indicative upper limit in terms of ^{40}K yields based on the current simulations. The $10 \times D_{3\text{D-insp.}}$ case ejects $3.992 \times 10^{-2}\text{ M}_{\odot}$, $3.054 \times 10^{-3}\text{ M}_{\odot}$ and $9.857 \times 10^{-4}\text{ M}_{\odot}$ of ^{39}K , ^{40}K and ^{41}K , respectively.

Although this needs to be investigated further, it is likely that the occurrence of O-C shell mergers and the associated strong boost in ^{40}K is taking place in a significant fraction of but not all massive stars (C. Ritter et al. 2018a), and when it happens, likely with variable strength. To some degree the latter is reflected by the different assumed entrainment rates. Such efficient, yet variable production can introduce a heterogeneous signature of ^{40}K in the local ISM once the CCSN explodes, in addition to other K sources in GCE. In Fig. 11, we show the dispersion of K isotopic ratios in the ISM resulting from pollution by two single CCSN explosions, using the yields just provided and assuming a solar-like ISM composition. For each CCSN pollution scenario, we generated a random distribution of 10,000 points, considering a factor of 3 uncertainty in the K isotopic yields and a range of dilutions from $2 \times 10^3\text{ M}_{\odot}$ (lower limit derived for a low-energy CCSN, A. P. Ji et al. 2020) to a typical value of 10^5 M_{\odot} of ISM material. The obtained $^{41}\text{K}/^{39}\text{K}$ dispersions are less than 10% using the model

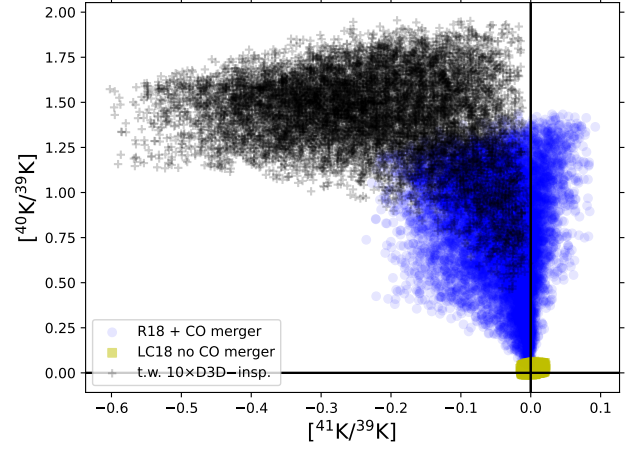


Figure 11. Predicted dispersion of K isotopic ratios in the interstellar medium (ISM) resulting from pollution by a single CCSN explosion, based on stellar yields from a 15 M_{\odot} star at solar metallicity with O-C shell merger (R18, C. Ritter et al. 2018a) and without (LC18 M. Limongi & A. Chieffi 2018), as well as shell-merger only predictions from this work (t.w.) for the $10 \times D_{3\text{D-insp.}}$ mixing case with an ingestion rate of $4 \times 10^{-3}\text{ M}_{\odot}$. Isotopic ratios are expressed in bracket notation, reported as logarithms base 10, and normalized to solar values.

without O-C shell merger and up to about a factor of two for the model with O-C shell merger by C. Ritter et al. (2018a). Similar variations could also be expected in the solar neighborhood due to GCE effects, such as different metal enrichment histories in the disk (e.g., V. Hegedűs et al. 2025, and references therein) and stellar migration (e.g., M. Kubryk et al. 2015). If instead we consider the $10 \times D_{3\text{D-insp.}}$ mixing case presented in the previous sections, we obtain a variation up to a factor of 4 from the solar $^{41}\text{K}/^{39}\text{K}$ ratio.

On the other hand, local ISM pollution from the CCSN model by C. Ritter et al. (2018a) would generate a $^{40}\text{K}/^{39}\text{K}$ dispersion up to a factor of 20. Likewise, the $10 \times D_{3\text{D-insp.}}$ mixing case from this work would produce an even larger dispersion, up to about a factor of 100, while the model without O-C shell merger would show again an insignificant dispersion. Note, that we are showing in this way only the $10 \times D_{3\text{D-insp.}}$ mixing case, which is the one with the largest ^{40}K production but not the one with the largest $^{40}\text{K}/^{39}\text{K}$ ratio (Fig. 8). The latter is obtained for the 1 and $3 \times D_{3\text{D-insp.}}$ mixing cases.

The show-cased O-C shell merger cases would introduce a strongly heterogeneous signature in the GCE K abundances of the ISM, locally decoupling the abundance of ^{40}K from the other K isotopes obtained from GCE. Consequently, the Sun cannot be used as a ro-

bust reference for the $^{40}\text{K}/\text{K}$ ratio for stars in the solar neighborhood. Instead, our work shows that solar “twins” with otherwise similar metallicity and K abundance could have significantly different initial ^{40}K abundance compared to the solar system. The ^{40}K isotopic effect described here has important thermal histories for rocky exoplanets. Energy produced from natural radioactive decay and the leftover primordial heat from planet formation powers the (internal) geodynamics of a rocky planet like Earth. Rocky planet mantle temperatures govern, for example, magmatism and crustal compositions, style of (L. H. Rüpke et al. 2004) and tectonic regime (e.g., C. O’Neill et al. 2016; M. Brown et al. 2020)

Thermal evolution models offer a unique approach to understanding the evolution of temperatures within rocky planetary interiors (Earth, Venus, Mercury, Mars, large asteroids, icy moons, trans-neptunian objects, and ‘terrestrial-type’ exoplanets). These models are used to constrain their volcanism and surface geology. Subordinate lithophile elements such as K and Cl also help stabilize minerals that control bulk transport properties, and/or volatile transport in rocky crusts and mantles (H. Fei et al. 2017; M. Nishi et al. 2014; M. G. Pamato et al. 2015; W. Xu et al. 2008). A rocky planet’s internal heat production is a function of potential and kinetic energy released during accretion and core formation, and radioactive decay (cf. S. Labrosse & C. Jaupart 2007) thus, mantle heat production depends on planet(star) age. A planet’s ability to sustain a mantle convective regime and crustal processes changes considerably with its evolving thermal profile due to cooling over geologic timescales of billions of years (L. Noack & D. Breuer 2014; N. H. Sleep 2000; C. T. Unterborn et al. 2018). Here, we have shown that across different extra-solar systems we can expect the starting inventories of these nuclides to vary in abundance, including in their isotopes such as ^{40}K even if the elemental abundances may be similar to Solar. Despite the long-suspected (but hitherto, unconstrained) variability, the majority of exoplanet studies up to now have applied Solar values for radionuclide (U, Th, K) concentrations, often without considering the decay after planet formation (E. A. Frank et al. 2014).

As an example, we illustrate this in Fig. 12, which shows the heating rate over time for Earth. To mimic the ^{40}K variations observed in Fig. 11, we multiply and divide the current abundance of ^{40}K in Earth’s silicate mass (3.04×10^{-8} kg/kg, e.g. E. A. Frank et al. 2014, and references therein) by a factor of 3. Although similar terawatt (TW) values are obtained today by varying

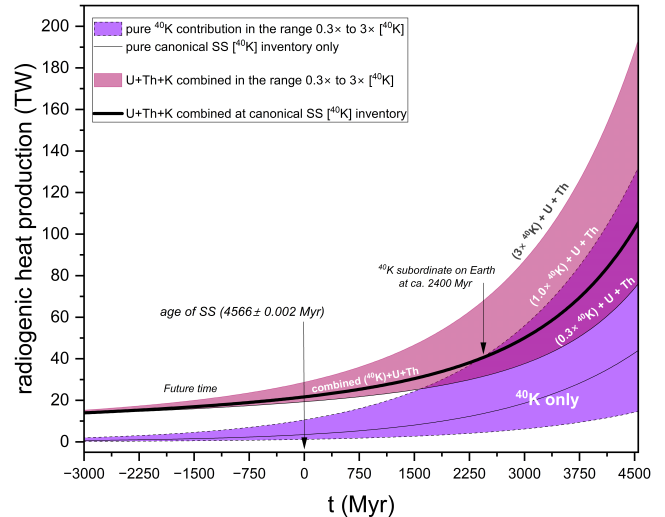


Figure 12. The evolution over time of the radioactive heat production is shown for an Earth-like planet, where ^{40}K abundances are increased and decreased by a factor of 3 compared to the typical Earth values. The combined total heat productions by ^{40}K , ^{232}Th , ^{235}U , and ^{238}U are also shown. Time on the x-axis is in Myr before present and so moves from right to left.

the ^{40}K abundance, the planet’s heating history would clearly be significantly different.

We will explore in detail elsewhere the implications of this for different types of rocky planets, considering more detailed pollution scenarios. Indeed, it is unclear whether the Solar System has a $^{40}\text{K}/\text{K}$ ratio consistent with GCE or if it reflects local pollution from CCSNe. Another interesting aspect, beyond the scope of this analysis, is whether we should expect local variations in the other radioactive sources, U and Th. The current GCE of Th in the Milky Way disk is under debate (e.g., R. B. Botelho et al. 2019; T. Mishenina et al. 2022), while measuring U in stellar spectra is even more challenging. Since r -process sources are expected to be much rarer than CCSNe (e.g., C. Sneden et al. 2008; J. J. Cowan et al. 2021), heterogeneous signatures from local $^{235,238}\text{U}$ and ^{232}Th pollution are likely to be extremely rare and possibly directly associated with the stellar Th abundance. However, the relevance of such heterogeneity affecting also the r -process actinide abundances cannot be ruled out. It is worth noting that a significant ^{244}Pu abundance enhancement, where ^{244}Pu is a short-lived radioactive isotope also made by the r process, can be inferred for the Early Solar System compared to measurements representative of the present ISM, derived from deep-sea crust and other planetary materials (e.g., K. Hotokezaka et al. 2015; A. Wallner et al. 2021;

B. Wehmeyer et al. 2023; X. Wang et al. 2023; S. Bishop et al. 2025).

5. DISCUSSIONS AND CONCLUSIONS

As shown in this analysis, O-C shell mergers significantly modify the pre-explosive yields of the light odd-Z elements, particularly elemental K which can be enhanced by up to $38\times$ compared to C. Ritter et al. (2018b). Mixing conditions are set by the 3D macro physics of convection of the O-C shell merger and strongly affects the production of ^{40}K , which is a long-lived radionuclide with a half-life of $t_{1/2} = 1.248$ Gyr that contributes to radiogenic heating in planets (E. A. Frank et al. 2014; C. O'Neill et al. 2020). Not only is the elemental K enhanced, but so is $^{40}\text{K}/\text{Fe}$ up to $20\times$ compared to C. Ritter et al. (2018b) result for the $10 \times D_{3\text{D-insp.}}$ mixing case with an ingestion rate of $4 \times 10^{-3} \text{ M}_{\odot} \text{ s}^{-1}$ (using square bracket notation adding the results of Fig. 6 and Fig. 8). This would mean that the ^{40}K contributed to GCE is significantly enhanced. As we showed in Fig. 11, there is a large variation in the $^{40}\text{K}/^{39}\text{K}$ ratio which tracks the $^{40}\text{K}/\text{K}$ ratio as ^{39}K is the dominant isotope of K. This combined with the fact that the mixing conditions do not non-monotonically affect the production of ^{39}K and ^{40}K means that the $^{40}\text{K}/^{39}\text{K}$ ratio can vary significantly between stars with otherwise similar metallicity and elemental K observations, which brings into question the validity of deriving ^{40}K from an elemental abundance measurement of the host star. Furthermore, we have shown that the production of ^{40}K in O-C shell mergers is so high that it could potentially introduce heterogeneous signatures in the local ISM. With the reference CCSN model considered in in this work, we find that ^{40}K could be enhanced by up to a factor of 20 compared to its background GCE abundance, decoupling the ^{40}K abundance from the observable K abundances resulting from GCE. With the most ^{40}K -rich mixing model discussed in this work, we find possible heterogenous signatures affecting all K isotopes, with a ^{40}K -enhancement up to a factor of a hundred.

An enhanced ^{40}K would have a significant effect on the history of radiogenic heat production in the mantle of an Earth-like planet. A higher initial inventory of ^{40}K raises the radiogenic heat budget and sustains vigorous mantle convection and melt production for longer, which in turn prolongs outgassing and delays tectonic/volcanic shutdown. Thermal-chemical evolution models show that increased internal heating can keep silicate planets volcanically and climatically active for Gyr timescales beyond nominal cases by maintaining continuous outgassed supply to the atmosphere and postponing secular cooling (B. J. Foley & A. J. Smye 2018; E. A. Frank et al.

2014). In our context, a $\sim 2\times$ enhancement in ^{40}K plausibly extends the duration of high outgassing and temperate surface conditions into later epochs relative to an Earth twin, while a $\sim 10\times$ case would push the system toward a long-lived super-volcanic regime (still buffered by the carbon-silicate feedback), thereby broadening the temporal window for habitability via sustained greenhouse forcing and volatile cycling (B. J. Foley & A. J. Smye 2018).

An elevated ^{40}K budget implies persistently high volcanic fluxes and a greater frequency of large eruptions. Time-variable outgassing (e.g., SO_2 pulses that rapidly convert to sulfate aerosols) imprints may be detectable, *time-dependent* changes in atmospheric composition—most notably in O_3 and H_2O bands—on Earth-like exoplanets (C. Ostberg et al. 2023). Multi-epoch direct imaging/spectroscopy with future facilities such as the Habitable Worlds Observatory may therefore have the potential to discriminate a super-volcanic, high- ^{40}K Earth-analog from a more quiescent twin (P. Liggins et al. 2022b; C. Ostberg et al. 2023).

Although our results demonstrate that mixing conditions strongly influence the production of the light odd-Z elements, they do not yet provide a complete picture. Our analysis examines a single stellar model at $Z = 0.02$, and as Table 1 shows that in the O-C merger region final mass fraction of ^{39}K can vary by a factor of 3, ^{40}K by a factor of 16, and ^{41}K by a factor of 38 between the four merger models from C. Ritter et al. (2018b). Model differences are not as impactful as mixing conditions, however, as §3.2 shows that final production of ^{39}K , ^{40}K , and ^{41}K in the O shell can vary by a factor of 263, 2340, and 204 respectively across all mixing cases.

Our results in Figures 4–8 omits the subsequent core-collapse supernova and any explosive nucleosynthesis that may occur, and uses a first-order approximation to estimate the final yields. The post-processing approach does not properly account for the evolution of the merger in the 1D model, as temperature and density evolve and we do not simulate the mixing of material in the O shell up into the merged C shell. Further, it is not clear what the length of the merger would be in 3D nor its behaviour for energy feedback in response to the burning of ingested fuel, such as the recently identified SPAR process (L. Roberti & M. Pignatari 2025). While these approximations limit presently the accuracy of specific quantitative predictions, the result presented here, that 3D macro physics mixing conditions strongly affect the nucleosynthesis, is robust. We also demonstrated that the 1D mixing prescriptions used here do not capture the full range of possible mixing behaviours that may occur in 3D.

Additionally, one would expect the MLT $4 \times 10^{-3} \text{ M}_{\odot} \text{s}^{-1}$ mixing case to match the C. Ritter et al. (2018b) model most closely in Figures 4–8. The difference results from a combination of the above factors and possibly also that in our targeted, zoom-in post-processing we took great care that temporal and spatial resolution is sufficient to resolve the convective-reactive nucleosynthesis, which cannot be expected from survey stellar evolution models as those by C. Ritter et al. (2018b). This highlights the difficulty of capturing convective-reactive events in 1D stellar evolution models and the need for 3D hydrodynamic simulations to inform 1D models.

The highest priority, therefore, is to investigate the macro physics of O-C shell mergers with fully 3D hydrodynamic simulations. Such simulations must quantify the mixing, identify feedback mechanisms, and establish when and how often mergers occur. Ultimately, full stellar-evolution calculations with mixing prescriptions calibrated to these 3D simulations are needed to assess the impact of mixing conditions on pre-supernova and ejecta yields, and inform planetary science studies of the impact of ^{40}K on planetary thermal histories and ultimately habitability.

ACKNOWLEDGMENTS

FH is supported by a Natural Sciences and Engineering Research Council of Canada (NSERC) Discovery Grant and acknowledges support from the NSERC award SAPPJ-797 2021-00032 *Nuclear physics of the dynamic origin of the elements*. We acknowledge support from the ChETEC-INFRA project funded by the European Union’s Horizon 2020 Research and Innovation programme (Grant Agreement No 101008324). This research has used the Astrophub online virtual research environment

(<https://astrophub.uvic.ca>), developed and operated by the Computational Stellar Astrophysics group at the University of Victoria and hosted on the Digital Research Alliance of Canada Arbutus Cloud at the University of Victoria. This work benefited from interactions and workshops co-organized by The Center for Nuclear astrophysics Across Messengers (CeNAM) which is supported by the U.S. Department of Energy, Office of Science, Office of Nuclear Physics, under Award Number DE-SC0023128. MP acknowledges the support to NuGrid from the “Lendulet-2023” Program of the Hungarian Academy of Sciences (LP2023-10, Hungary), the ERC Consolidator Grant funding scheme (Project RADIOSTAR, G.A. n. 724560, Hungary), the ChETEC COST Action (CA16117), supported by the European Cooperation in Science and Technology, and the IReNA network supported by NSF AccelNet (Grant No. OISE-1927130). MP also thanks the support from NKFI via K-project 138031 (Hungary). SJM and MP acknowledge funding from the ERC Horizon Europe funding programme in support of the Synergy Grant - Geoastronomy, grant agreement number 101166936. SJM also thanks the BGI/University of Bayreuth in Germany for hosting the Geoastronomy Research Group.

AUTHOR CONTRIBUTIONS

JJ performed the simulations, analyzed the results, and wrote the manuscript. FH provided guidance and support for the project and edited the manuscript. MP calculated the impact of heterogeneous mixing in the ISM of K isotopes, participating in data analysis and in writing the manuscript. SM computed the differential heat production of variable starting ^{40}K abundances, participating in data analysis, and in writing the manuscript.

Software: Data is available on <https://astrophub.uvic.ca>.

REFERENCES

- Andrassy, R., Herwig, F., Woodward, P., & Ritter, C. 2020, Monthly Notices of the Royal Astronomical Society, 491, 972, doi: [10.1093/mnras/stz2952](https://doi.org/10.1093/mnras/stz2952)
- Asplund, M., Grevesse, N., Sauval, A. J., & Scott, P. 2009, Annual Review of Astronomy and Astrophysics, 47, 481, doi: [10.1146/annurev.astro.46.060407.145222](https://doi.org/10.1146/annurev.astro.46.060407.145222)
- Bishop, S., Stanciu, I., Cabré, A., et al. 2025, PSJ, 6, 75, doi: [10.3847/PSJ/adbbd6](https://doi.org/10.3847/PSJ/adbbd6)
- Botelho, R. B., Milone, A. d. C., Meléndez, J., et al. 2019, MNRAS, 482, 1690, doi: [10.1093/mnras/sty2791](https://doi.org/10.1093/mnras/sty2791)
- Brown, M., Johnson, T., & Gardiner, N. J. 2020, Annual Review of Earth and Planetary Sciences, 48, 291, doi: [10.1146/annurev-earth-081619-052705](https://doi.org/10.1146/annurev-earth-081619-052705)
- Cowan, J. J., Sneden, C., Lawler, J. E., et al. 2021, Reviews of Modern Physics, 93, 015002, doi: [10.1103/RevModPhys.93.015002](https://doi.org/10.1103/RevModPhys.93.015002)
- Davis, A., Jones, S., & Herwig, F. 2018, Monthly Notices of the Royal Astronomical Society, 484, 3921, doi: [10.1093/mnras/sty3415](https://doi.org/10.1093/mnras/sty3415)
- Fei, H., Huang, R., & Yang, X. 2017, Geophysical Research Letters, 44, 10226, doi: [10.1002/2017GL075070](https://doi.org/10.1002/2017GL075070)

- Fischer, T. P., & Aiuppa, A. 2020, *Annual Review of Earth and Planetary Sciences*, 48, 529, doi: [10.1146/annurev-earth-053018-060321](https://doi.org/10.1146/annurev-earth-053018-060321)
- Foley, B. J., & Smye, A. J. 2018, *Astrobiology*, 18, 873, doi: [10.1089/ast.2017.1695](https://doi.org/10.1089/ast.2017.1695)
- Frank, E. A., Meyer, B. S., & Mojzsis, S. J. 2014, *Icarus*, 243, 274, doi: [10.1016/j.icarus.2014.08.031](https://doi.org/10.1016/j.icarus.2014.08.031)
- Frank, E. A., Meyer, B. S., & Mojzsis, S. J. 2014, *Icarus*, 243, 274, doi: [10.1016/j.icarus.2014.08.031](https://doi.org/10.1016/j.icarus.2014.08.031)
- Frank, E. A., Meyer, B. S., & Mojzsis, S. J. 2014, *Icarus*, 243, 274, doi: [10.1016/j.icarus.2014.08.031](https://doi.org/10.1016/j.icarus.2014.08.031)
- Freytag, B., Ludwig, H. G., & Steffen, M. 1996, *Astronomy and Astrophysics*, 313, 497
- Hegedűs, V., Mészáros, S., Világos, B., et al. 2025, *A&A*, 699, A293, doi: [10.1051/0004-6361/202553951](https://doi.org/10.1051/0004-6361/202553951)
- Herwig, F. 2000, *The Evolution of AGB Stars with Convective Overshoot*, arXiv, doi: [10.48550/arXiv.astro-ph/0007139](https://doi.org/10.48550/arXiv.astro-ph/0007139)
- Herwig, F., Woodward, P. R., Lin, P.-H., Knox, M., & Fryer, C. 2014, *The Astrophysical Journal Letters*, 792, L3, doi: [10.1088/2041-8205/792/1/L3](https://doi.org/10.1088/2041-8205/792/1/L3)
- Hotokezaka, K., Piran, T., & Paul, M. 2015, *Nature Physics*, 11, 1042, doi: [10.1038/nphys3574](https://doi.org/10.1038/nphys3574)
- Issa, J., Herwig, F., Denissenkov, P., & Pignatari, M. 2025, *Impact of 3D Macro Physics and Nuclear Physics on the p Nuclei in O-C Shell Mergers*, arXiv, doi: [10.48550/arXiv.2507.16965](https://doi.org/10.48550/arXiv.2507.16965)
- Ji, A. P., Li, T. S., Simon, J. D., et al. 2020, *ApJ*, 889, 27, doi: [10.3847/1538-4357/ab6213](https://doi.org/10.3847/1538-4357/ab6213)
- Jones, S., Andrassy, R., Sandalski, S., et al. 2017, *Monthly Notices of the Royal Astronomical Society*, 465, 2991, doi: [10.1093/mnras/stw2783](https://doi.org/10.1093/mnras/stw2783)
- Kobayashi, C., Karakas, A. I., & Lugaro, M. 2020, *The Astrophysical Journal*, 900, 179, doi: [10.3847/1538-4357/abae65](https://doi.org/10.3847/1538-4357/abae65)
- Korenaga, J. 2008, *Terra Nova*, 20, 419, doi: [10.1111/j.1365-3121.2008.00843.x](https://doi.org/10.1111/j.1365-3121.2008.00843.x)
- Kubryk, M., Prantzos, N., & Athanassoula, E. 2015, *A&A*, 580, A126, doi: [10.1051/0004-6361/201424171](https://doi.org/10.1051/0004-6361/201424171)
- Labrosse, S., & Jaupart, C. 2007, *Earth and Planetary Science Letters*, 260, 465, doi: [10.1016/j.epsl.2007.05.046](https://doi.org/10.1016/j.epsl.2007.05.046)
- Liggins, P., Jordan, S., Rimmer, P. B., & Shorttle, O. 2022a, *Journal of Geophysical Research: Planets*, 127, e2021JE007123, doi: [10.1029/2021JE007123](https://doi.org/10.1029/2021JE007123)
- Liggins, P., Jordan, S., Rimmer, P. B., & Shorttle, O. 2022b, *Journal of Geophysical Research: Planets*, 127, e2021JE007123, doi: [10.1029/2021JE007123](https://doi.org/10.1029/2021JE007123)
- Limongi, M., & Chieffi, A. 2018, *ApJS*, 237, 13, doi: [10.3847/1538-4365/aac234](https://doi.org/10.3847/1538-4365/aac234)
- Meakin, C. A., & Arnett, D. 2006, *The Astrophysical Journal*, 637, L53, doi: [10.1086/500544](https://doi.org/10.1086/500544)
- Meakin, C. A., & Arnett, D. 2007, *The Astrophysical Journal*, 667, 448, doi: [10.1086/520318](https://doi.org/10.1086/520318)
- Mishenina, T., Pignatari, M., Gorbaneva, T., et al. 2022, *MNRAS*, 516, 3786, doi: [10.1093/mnras/stac2361](https://doi.org/10.1093/mnras/stac2361)
- Mishenina, T., Pignatari, M., Côté, B., et al. 2017, *MNRAS*, 469, 4378, doi: [10.1093/mnras/stx1145](https://doi.org/10.1093/mnras/stx1145)
- Nishi, M., Irifune, T., Tsuchiya, J., et al. 2014, *Nature Geoscience*, 7, 224, doi: [10.1038/NGEO2074](https://doi.org/10.1038/NGEO2074)
- Noack, L., & Breuer, D. 2014, *Planetary and Space Science*, 98, 41, doi: [10.1016/j.pss.2013.06.020](https://doi.org/10.1016/j.pss.2013.06.020)
- Noack, L., & Breuer, D. 2014, *Planet. Space Sci.*, 98, 41, doi: [10.1016/j.pss.2013.06.020](https://doi.org/10.1016/j.pss.2013.06.020)
- O'Neill, C., Lenardic, A., Weller, M., et al. 2016, *Physics of the Earth and Planetary Interiors*, 255, 80, doi: [10.1016/j.pepi.2016.04.002](https://doi.org/10.1016/j.pepi.2016.04.002)
- O'Neill, C., Lowman, J., & Wasiliev, J. 2020, *Icarus*, 352, 114025, doi: [10.1016/j.icarus.2020.114025](https://doi.org/10.1016/j.icarus.2020.114025)
- Ortenzi, G., Noack, L., Sohl, F., et al. 2020, *Scientific Reports*, 10, 10907, doi: [10.1038/s41598-020-67751-7](https://doi.org/10.1038/s41598-020-67751-7)
- Ostberg, C., Wolf, E. T., Kopparapu, R. K., et al. 2023, *The Astronomical Journal*, 166, 206, doi: [10.3847/1538-3881/acec0e](https://doi.org/10.3847/1538-3881/acec0e)
- Pamato, M. G., Myhill, R., Ballaran, T. B., et al. 2015, *Nature Geoscience*, 8, 75, doi: [10.1038/NGEO2306](https://doi.org/10.1038/NGEO2306)
- Paxton, B., Bildsten, L., Dotter, A., et al. 2010, *The Astrophysical Journal Supplement Series*, 192, 3, doi: [10.1088/0067-0049/192/1/3](https://doi.org/10.1088/0067-0049/192/1/3)
- Pignatari, M., Herwig, F., Hirschi, R., et al. 2016, *The Astrophysical Journal Supplement Series*, 225, 24, doi: [10.3847/0067-0049/225/2/24](https://doi.org/10.3847/0067-0049/225/2/24)
- Prantzos, N., Abia, C., Limongi, M., Chieffi, A., & Cristallo, S. 2018, *MNRAS*, 476, 3432, doi: [10.1093/mnras/sty316](https://doi.org/10.1093/mnras/sty316)
- Rauscher, T., Heger, A., Hoffman, R. D., & Woosley, S. E. 2002, *The Astrophysical Journal*, 576, 323, doi: [10.1086/341728](https://doi.org/10.1086/341728)
- Ritter, C., Andrassy, R., Côté, B., et al. 2018a, *Monthly Notices of the Royal Astronomical Society*, 474, L1, doi: [10.1093/mnrasl/slx126](https://doi.org/10.1093/mnrasl/slx126)
- Ritter, C., Herwig, F., Jones, S., et al. 2018b, *Monthly Notices of the Royal Astronomical Society*, 480, 538, doi: [10.1093/mnras/sty1729](https://doi.org/10.1093/mnras/sty1729)
- Rizzuti, F., Hirschi, R., Varma, V., et al. 2024, *Monthly Notices of the Royal Astronomical Society*, 533, 687, doi: [10.1093/mnras/stae1778](https://doi.org/10.1093/mnras/stae1778)
- Roberti, L., & Pignatari, M. 2025, *The SPAr Process: Proton Captures Powering Carbon-Oxygen Shell Mergers in Massive Stars*, doi: [10.48550/arXiv.2509.13749](https://doi.org/10.48550/arXiv.2509.13749)

- Roberti, L., Pignatari, M., Brinkman, H. E., et al. 2025, The Occurrence and Impact of Carbon-Oxygen Shell Mergers in Massive Stars, arXiv
- Rüpke, L. H., Morgan, J. P., Hort, M., & Connolly, J. A. D. 2004, 223, 17, doi: [10.1016/j.epsl.2004.04.018](https://doi.org/10.1016/j.epsl.2004.04.018)
- Sleep, N. H. 2000, *Journal of Geophysical Research: Planets*, 105, 17563, doi: [10.1029/2000JE001240](https://doi.org/10.1029/2000JE001240)
- Snedden, C., Cowan, J. J., & Gallino, R. 2008, *ARA&A*, 46, 241, doi: [10.1146/annurev.astro.46.060407.145207](https://doi.org/10.1146/annurev.astro.46.060407.145207)
- Spaargaren, R. J., Wang, H. S., Mojszis, S. J., Ballmer, M. D., & Tackley, P. J. 2023, *The Astrophysical Journal*, 948, 53, doi: [10.3847/1538-4357/acac7d](https://doi.org/10.3847/1538-4357/acac7d)
- Unterborn, C. T., Desch, S. J., Hinkel, N. R., & Lorenzo, A. 2018, *Nature Astronomy*, 2, 297, doi: [10.1038/s41550-018-0411-6](https://doi.org/10.1038/s41550-018-0411-6)
- Wallner, A., Froehlich, M. B., Hotchkis, M. A. C., et al. 2021, *Science*, 372, 742, doi: [10.1126/science.aax3972](https://doi.org/10.1126/science.aax3972)
- Wang, X., Clark, A. M., Ellis, J., et al. 2023, *ApJ*, 948, 113, doi: [10.3847/1538-4357/acbeaa](https://doi.org/10.3847/1538-4357/acbeaa)
- Wehmeyer, B., López, A. Y., Côté, B., et al. 2023, *ApJ*, 944, 121, doi: [10.3847/1538-4357/acafec](https://doi.org/10.3847/1538-4357/acafec)
- Xu, W., Lithgow-Bertelloni, C., Stixrude, L., & Ritsema, J. 2008, *Earth and Planetary Science Letters*, 275, 70, doi: [10.1016/j.epsl.2008.08.012](https://doi.org/10.1016/j.epsl.2008.08.012)
- Yadav, N., Müller, B., Janka, H. T., Melson, T., & Heger, A. 2020, *The Astrophysical Journal*, 890, 94, doi: [10.3847/1538-4357/ab66bb](https://doi.org/10.3847/1538-4357/ab66bb)